This is the Pre-Published Version.
This is the peer reviewed version of the following article: Huang, L., Yang, T., Wong, L. W., Zheng, F., Chen, X., Lai, K. H., ... & Ly, T. H. (2021). Redox photochemistry on van der Waals surfaces for reversible doping in 2D materials. Advanced Functional Materials, 31(16), 2009166, which has been published in final form at https://doi.org/10.1002/adfm.202009166. This article may be used for non-commercial purposes in accordance with Wiley Terms and Conditions for Use of Self-Archived Versions. This article may not be enhanced, enriched or otherwise transformed into a derivative work, without express permission from Wiley or by statutory rights under applicable legislation. Copyright notices must not be removed, obscured or modified. The article must be linked to Wiley's version of record on Wiley Online Library and any embedding, framing or otherwise making available the article or pages thereof by third parties from platforms, services and websites other than Wiley Online Library must be prohibited.
The following publication Huang, L., Yang, T., Wong, L. W., Zheng, F., Chen, X., Lai, K. H., ... & Ly, T. H. (2021). Redox photochemistry on van der Waals surfaces for reversible doping in 2D materials. Advanced Functional Materials, 31(16), 2009166 is available at https://doi.org/10.1002/adfm.202009166

Redox photochemistry on van der Waals surfaces for reversible doping in two-dimensional materials

Lingli Huang, Tiefeng Yang, Lok Wing Wong, Fangyuan Zheng, Xin Chen, Ka Hei Lai, Haijun Liu, Quoc Huy Thi, Dong Shen, Chun-Sing Lee, Qingming Deng, Jiong Zhao*, Thuc Hue Ly**
L. Huang, T. Yang, X. Chen, H. Liu, Q. H. Thi, D. Shen, C.-S. Lee, T. H. Ly

Department of Chemistry and Center of Super-Diamond & Advanced Films
City University of Hong Kong
Kowloon, Hong Kong, P. R. China
E-mail: thuchly@cityu.edu.hk

L. Huang, X. Chen, H. Liu, Q. H. Thi, T. H. Ly

City University of Hong Kong Shenzhen Research Institute
Shenzhen 518000, China

L. W. Wong, F. Zheng, K. H. Lai, J. Zhao
Department of Applied Physics
The Hong Kong Polytechnic University
Kowloon, Hong Kong, China
E-mail: jiongzhao@polyu.edu.hk

L. W. Wong, F. Zheng, K. H. Lai, J. Zhao
The Hong Kong Polytechnic University Shenzhen Research Institute
Shenzhen 518000, China

Q. Deng
Physics department and Jiangsu Key Laboratory for Chemistry of Low-Dimensional Materials
Huaiyin Normal University,
Huaian 223300, China
E-mail: qingmingdeng@gmail.com

Keywords: (redox, photochemistry, two-dimensional materials, anisotropic, reversible doping)

Abstract
Despite the van der Waals (vdW) surfaces are usually chemically inert, we introduce an un-destructive, scalable and reversible redox reactions on the vdW surfaces of two-dimensional (2D) anisotropic semiconductors ReX_2 (X=S or Se) facilitated by simple photochemistry. Ultraviolet (UV) light (with humid) and laser exposure can reversibly oxidize and reduce rhenium disulfide (ReS_2) and rhenium diselenide ($ReSe_2$), respectively, yielding pronounced

doping effect with good control. Evidenced by Raman spectroscopy, dynamic force microscopy (DFM), transmission electron microscopy (TEM) and X-ray photoelectron spectroscopy (XPS) the grafting and removal of covalently functionalized oxygen groups on the perfect vdW surfaces has been confirmed. The optical and electrical properties can be thereby reversibly tunable in wide ranges. Such optical direct-writing and rewritable capability via solvent/contaminant-free approach for chemical doping is compelling in the coming era of 2D materials.

Main Text

Doping is the key for tuning the properties of semiconductors. The recent emergence of two-dimensional (2D) materials,[1] such as graphene and transition metal dichalcogenides (TMDs) can potentially revolutionize future electronics. While excellent in stability, flexibility, sensitivity and carrier mobility for these 2D materials, due to the chemical inertness of van der Waals (vdW) surfaces, lack of chemical doping on demand is currently impeding the technological development.[2] The alternative electrostatic,[3] or ionic liquid gating,[4] methods have drawbacks in lifetime or scaling.[5] The present chemical doping in 2D materials,[6] predominantly enrolled defects, potentially hampering the stability and reproducibility.

Since the surge of tremendous interests in 2D materials, different techniques especially the chemical vapor deposition (CVD) have been proposed for the large-scale synthesis.[7] Particularly, successful realization of various in-plane or vertical 2D heterostructures and alloys have well shown the rapid development towards the ultimate atomic-scale design and constructions.[6] Some works have also reported phase engineering on the polymorphic 2D materials, [8] which are of great potentials for integrable and rewritable electronics and memory device. However, in the perspective of most electronic or optoelectronic applications, precise n- or p- type doping at controllable locations in semiconductors is indispensable for device fabrication. In this connection, possibilities have been opened up for the post-synthesis chemical doping,[9] or functionalizations in several 2D materials.[10] Owing to the ultrathin

thickness and the reactive nature at defect sites in 2D materials, lack of control and stability become major challenges for the doping in 2D materials.[11]

Defect functionalizations in graphene,[9] molybdenum disulfide (MoS_2),[10] or other 2D materials,[11] usually mean severe and irreversible degradation in structures and performances. Thus far, except for the hydrogenated graphene,[12] homogeneous direct covalent functionalization of dopant atoms on the perfect vdW surfaces of 2D materials has not been reported. Compared with the gapless graphene, controllable chemical doping for 2D semiconductors such as TMDs is even more demanding. Here we found the 2D semiconductors such as rhenium disulfide (ReS_2) and rhenium diselenide ($ReSe_2$), can be reversibly oxidized and reduced via covalent oxidation/reduction on vdW surface without generation/participation of atomic defects, yielding a highly scalable and industrially compatible chemical doping technology for 2D materials.

As members of TMD of the VIIB group materials, an extra electron results in distortion coordination to make ReS_2 and $ReSe_2$ stable with tetragonal (1T') structure and endows anisotropy.[13] Here, monolayer (1L) flakes of ReS_2 and $ReSe_2$ are grown via the atmospheric CVD system,[14] and transferred onto 300 nm SiO_2/Si substrate assisted by Poly (methyl methacrylate) (PMMA) (see Experimental Section).

First, we demonstrate the pristine 1L-ReS_2 can be reversibly oxidized and reduced via UV exposure and laser (633 nm) treatments, respectively (scheme shown in **Figure 1**a, see Experimental Section). Since the bi-stable pristine/oxidized 1L-ReS_2, we can further demonstrate the UV and laser exposure can be used for local patterning of the pristine/oxidized zones in 1L-ReS_2 at will, such as the nano "REDOX" pattern of pristine 1L-ReS_2 embedded in the oxidized 1L-ReS_2 (Figures 1b,c and S1). A series of Raman modes of 1L-ReS_2 in the range of 110 ~ 450 cm^{-1} are obtained under 30 s, 90 s, 180 s UV treatment followed by stepwise laser irradiation (Figure 1d). The Raman peak intensity drops dramatically and blue-shifts after sequential UV treatment, then reversed to the pristine peak intensity and position after further

laser irradiation. The evolving normalized Raman intensity, peak shift and intensity ratio (mode I at 153 cm^{-1} /mode II at 163 cm^{-1}) during a few cycles of UV-laser treatments are depicted in Figure 1e, extracted from fitted Raman peaks (see Figures S2 and S3). The 180 s UV treatment in our condition is able to cause the Raman intensities drop by 29% and 72% for mode I and II peaks, respectively, likewise, blue shift at 4.2 cm^{-1} and 5.3 cm^{-1} are triggered for mode I and II, respectively. The following laser irradiation (60 s) after UV treatment on the samples can completely recover the UV induced changes (Figure 1e).

The effects from specific conditions of UV and laser treatments, including the processing time, laser power and excitation wavelength are summarized in Figures S4-S7. Initially, there is no Raman enhancement on pristine ReS_2 under long time laser irradiation (633 nm, 6.11 mW), as shown in Figure S4. Futhermore, the recovery rate of Raman intenisty is proportional to the laser power (sees Figure S6) during UV/laser treatments. In addition, the reversible rate under 514 nm laser (0.54 mW) irradiation is 6.7-fold than that of under 633 nm laser (0.57 mW) as shown in Figure S7. Besides, we also investigate the transfer influence, substrate effect, the humidity dependences and thermal effect on Raman intensity reversibility of ReS_2 (see Figures S8-S12). The 1L-ReS_2 transferred on the 300 nm SiO_2/Si substrate and the fluorophlogopite mica substrate have similar recovery rate. During transfer process, the coupling between as-grown materials and substrates are released.[15] It results in the improvement of reversible doping performance on transferred ReS_2 comparing with as-grown ReS_2. Furthermore, the substrate effects mainly influence the optical (UV) reflection and adsorption of the ReS_2. After 180 s UV treatment, the Raman intensity at peak II of ReS_2 transferred onto SiO_2/Si substrate reduced to 3% of pristine, which suggests the ReS_2 on SiO_2/Si substrate suffered stronger oxidation (see Figure S9). It is attributed to the stronger optical reflection of SiO_2/Si substrate than the transparent fluoroplogopite mica substrate.[16] There are more oxygen radicals generated on the surface of ReS_2/SiO_2 during UV treatment. Further investigation shows that the humid level plays an imperative role in the oxidation degree of ReS_2. As shown in Figure

S10, the higher humid level results in heavier oxidation on the ReS_2 surface, denser of wrinkles and more reduction of Raman intensity. However, the recovery rate of Raman intensity does not be influenced by the humid level. Importantly, the UV-thermal annealing treatments are applied to investigate the thermal effect on Raman intensity reversibility (details in Figures S11 and S12). In fact, the thermal annealing (1st time) is efficient to restore the Raman intensity of UV treated ReS_2. The Raman intensity of UV treated ReS_2 is 100% recovered by thermal annealing (1st time). However, the Raman intensity is only recovered to 75% of pristine Raman intensity then starts to drop using thermal annealing whereas it is recovered to pristine intensity using laser irradiation after 180 s UV treatment (2nd time) (sees Figure S12). Overall, all of the as-grown and transferred ReS_2 exhibit the Raman intensity reversibility under UV treatment with variable humid level (30% ~ 80%) and laser irradiation with different wavelength and power. Additionally, the ReS_2 transferred onto SiO_2 wafer has the best reversibility. Likewise, a similar reversible oxidation/reduction effect by UV and laser treatments is also found in 1L-$ReSe_2$ (Figures 1f and S13-S15).

The undergoing structural changes related to Raman results above are unveiled by our DFM and TEM characterizations (see Experimental Section). In DFM topography images, the thickness of 1L-ReS_2 increases from 0.9 nm to 1.3 nm, and patterned wrinkles (few-hundred nm apart) with local height around 2.5 nm is formed after 180 s UV treatment (**Figure 2**a, b). After the following laser treatment, the wrinkles are barely seen (Figure 2c). Detailed topographic evolution and height profiles are provided in Figure S16. The surface roughness (RMS) is raised continuously during the 180 s UV treatment, and then drops after 60 s laser irradiation and fluctuates with 0.1 nm until the second period of UV treatment (Figure 2d). The wrinkle formation and relaxation imply the in-plane compressive strain after UV exposure and the release of strain after laser exposure. As a comparison, the thermal annealing is applied on UV treated 1L-ReS_2 to study the restore of the morphology by thermal effect (results as shown in Figures S17 and S18). As shown in Figure S18, the thickness of the flake decreases 0.1 nm,

the height of wrinkles reduces 0.5 nm and the width of wrinkles broadens 50 nm after thermal annealing (1st time). Correlated with the Raman intensity evolution, the Raman intensity is fully recovered by thermal annealing (1st time) whereas the morphology only restores slightly, which indicates the thermal annealing is not an efficient way to restore the morphology. In addition, the thickness of ReS_2 keeps at 1.0 nm at the following UV-thermal annealing treatments and the height of wrinkles decreases to 2.2 nm by thermal annealing (2nd time). The roughness (RMS) increases by UV treatment whereas keeps after thermal annealing. Differently, the wrinkles are flattened, the thickness of flake increases and roughness decreases using laser irradiation. Importantly, there are 0.8 nm deep cracks generated on the overall ReS_2 flake at the second UV-thermal annealing circle (sees Figure S18) meanwhile the Raman intensity starts to drop (sees Figure S12). As far as concerned, the laser irradiation is an efficient and non-destructive approach to release of wrinkles and strain.

Down to the atomic scale, high resolution scanning (S)TEM, energy dispersive spectroscopy (EDS) and electron energy loss spectroscopy (EELS) characterizations are employed. By EDS, we observe the oxygen content ramps steeply with the stable sulphur content after 180 s UV treatment (Figure 2e). EELS analysis on the original and UV treated 1L-ReS_2 show traces of oxygen and significant chemical shift in the S L edges caused by oxidation after UV treatment, corresponding to the formation of S-O bonding (Figure 2f). While the high resolution annular dark field (ADF) results (Figure 2g, h) exhibits no apparent structural changes in the 1L-ReS_2 after 180 s UV treatment, analysis in reciprocal space on the pristine and post-UV treatment samples show stark differences in intensities of reflexes corresponding to the T' phase superlattice structures (reflexes closest to origin) (Figure 2i, j). The reflexes in certain direction disappear after UV treatment, suggesting clear perturbations on the lattice periodicity by local bond distortions. The high resolution HAADF image (Figure 2k, l) analysis also renders similar conclusions that atomic distances in some locations are disturbed by the UV treatment (Figure 2m).

The UV (185 nm and 254 nm) light is known to be able to dissociate the moisture water and create abundant radicals through series of photochemical reactions (see Experimental Section).[17] According to our density functional theory (DFT) simulations, atomic structures of 1L-ReS_2 can be slightly distorted with the exotic covalently-bonded surface oxygen atoms(**Figure 3**a), in coincident with the above TEM results. After oxidation, two of the four crystallographically distinct S atoms in one unit cell in 1L-ReS_2 can have bonding lengths much shorter than the standard S-O bond, close to the S=O bond length (Figure S19), exhibiting the exceptional stability of such new bonds. The binding energy of S-O bond at 166.4 eV and adsorbed oxygen signal at 530.9 eV are evidenced using XPS at S 2p region and O 1s region, respectively (see Figure S20).[18] The ratio of S-O bond over S $2p_{1/2}$ and S $2p_{3/2}$ reduces ~ 4% after laser irradiation on ~ 1% area of ReS_2 which indicates the recovered doping effect. The excess electron in ReS_2 and $ReSe_2$ possibly renders the stronger oxygen affinity as compared to the electron-equilibrium counterpart like MoS_2. The textured wrinkles after UV exposure can be attributed to the expansion of basal plane lattice (up to *ca.* 2% along both ***a*** and ***b*** directions) (Figure 3b) after oxygen/hydroxyl functionalization. The formation energies for the oxygen and hydroxyl functionalization are 1.75 and 2.42 eV by DFT calculation, respectively, suggesting the oxidized products (Figure 3a, b) especially the hydroxyl groups on 1L-ReS_2 are robust against the ambient condition as compared to Pt (111) surface.[19] It is also interesting that the oxygen group is more stable than hydroxyl group on 1L-ReS_2, opposite to many other inorganic surfaces.[20]

Such stable vdW surface oxidation can be clearly observed in 1L-ReS_2 and 1L-$ReSe_2$, however absent in 1L-MoS_2 and graphene with our experimental conditions, where the defects are involved.[21] In MoS_2, the oxygen radicals could easily generate S vacancies instead of S-O bonding formation. Our DFT result shows the S vacancy formation energy of 1L-MoS_2 (-3.25 eV) is lower than that of 1L-ReS_2 (-2.55 eV), thus more likely to form vacancies during UV treatment in 1L-MoS_2 (see Figures S21 and S22), precluding the similar vdW surface oxidation

in MoS_2. DFT calculations also give the electronic structures of the products (Figure S23), showing new doping levels introduced by the acceptor dopants of oxygen. Depending on the original carrier types (n type mainly, see the electrical transport properties measurement results in **Figure** 4), the vdW surface oxidation by UV treatment can lead to either depletion of majority carriers (electrons) or hole injection, equal to p-doping in 1L-ReS_2. In opposite, the reduction or removal of oxygen groups by laser treatment conversely yields n-doping.

Therefore, it can be rationalized that Raman intensity reduction and blue shifts of peak I and II by UV exposure in 1L-ReS_2 is owing to the increased lattice disordering due to oxidation.[22] The increase of height (or layer thickness) after UV exposure by topography DFM is in line with the vdW surface grafting of functionalized groups. It is also shown by our technique that removal of oxygen functional groups on the 1L-ReS_2 surfaces can be controlled by laser annealing. Eventually, all the oxygen groups formed by UV can be removed by laser treatment and intrinsic 2D ReS_2 is restored. After the compressive strain in layer by oxidation is released by the laser annealing treatment, flat surfaces are recovered. The average flake height increase (not roughness) after laser treatment compared to pristine is possibly attributed to the flake delamination effect.[23] Using this UV-laser combined approach, we can easily pattern p-/n-doping zones using the pristine/oxidized 1L-ReS_2 with sub-μm precision (Figure 1b, c), exhibiting the great potential of this technique for device fabrication.

In light of the doping effects of surface covalent bonding, here we show two examples of application, the photochemical modulation on the photoluminescence (PL) property and electrical transport property in field effect transistor (FET) devices made of 1L-ReS_2. The PL results are presented in Figure 3c, while the PL evolution upon UV-laser treatments is summarized in Figure 3d (data extracted from Figure S24). Notably, the intensity decreases dramatically by 81% after the first cycle of UV treatment and then reversed to the pristine intensity (100%) after 60 s laser irradiation. The PL spectra are fitted using Lorentz curves, the bandgap exciton (A) and trion (A^-) for 1L-ReS_2 are responsible for the intrinsic PL emission.[24]

The reduction of PL intensity after UV treatment coincides with the p type doping effect and depletion of majority carriers in oxidized 1L-ReS_2.

Furthermore, we fabricated series of FET devices and sequentially tested the transport properties of pristine, UV oxidized and laser treated 1L-ReS_2 FET devices (Figure 4a, transfer curve shown in Figure 4b and output curve shown in Figure 4c). The performance changes of the FET devices upon 90 s UV and 60 s laser (633 nm, 0.57 mW) treatments are fully in agreement with the previously discussed p-doping effect by UV exposure and reverse to n-doping effect by the following laser annealing treatments. On average, the on-state channel current drops by 1-2 orders of magnitude after UV treatment compared with the pristine devices. The on-off ratio of the FETs increases from around 3×10^3 to over 10^4 after UV treatment. All the pristine devices showed n type doping behavior, thus the UV exposure (p-type doping) significantly reduces the carrier density, and the carrier mobility is dramatically decreased by 70-80% after UV oxidation due to the enhanced scattering by dopant atoms. After the following stepwise laser annealing on the channels, eventually all the carrier density, on-off ratio, mobility and threshold voltage can be brought back to the pristine states (Figure 4d). Tables S1-S3 have summarized the FET device measurements on the 1L-ReS_2 samples. The full FET device results and associated Raman spectroscopy results for the 1L ReS_2 channel in FET devices are shown in Figures S25-S30. In addition, if the UV treatment time is elongated from 90s to 180s, the apparent ambipolar transport behavior in the 1L-ReS_2 FET can be observed (see Figure S31), caused by the heavier p-doping under long time UV exposure. The observed reversible modulation on the electrical transport in these FET devices completely corroborated the aforementioned photochemical doping mechanisms.

In conclusion, we reported a reversible and robust chemical doping technique via direct vdW surface oxidation and reduction facilitated by simple UV and laser treatments on 2D anisotropic semiconductors, such as ReS_2 and $ReSe_2$. This photochemical approach without atomic defects involved are highly controllable and can effectively modulate the electrical, optical and

chemical properties in these 2D semiconductors. Moreover, the oxidized surfaces can facilitate further epi-layering, enriching the device structures. The successful chemical activation of vdW surfaces without atomic defects will also provide opportunities for further chemical functionalizations and relevant electrochemical applications. Therefore, this new strategy, which is entirely compatible with the current semiconductor industry, paves new way for the future designing and scaling of 2D devices.

Experimental Section

Synthesis of rhenium disulphide (ReS_2), rhenium diselenide ($ReSe_2$) and molybdenum disulphide (MoS_2): The monolayer (1L) ReS_2, $ReSe_2$ and MoS_2 are grown using the atmospheric chemical vapour deposition (CVD) system. Ammonium perrhenate (NH_4ReO_4) (Aldrich, 99.999%) and sulphur powder (Aldrich, 99.998%) with weight ratio 1 : 50, NH_4ReO_4 and selenium pellets (Aldrich, > 99.99%) with weight ratio 1 : 10, sodium molybdate ($Na_2MoO_4 \cdot 2H_2O$) (Aldrich, > 98%) and sulphur powder with weight ratio 1 : 2 are used as ReS_2, $ReSe_2$ and MoS_2 growth precursors, respectively. The precursor of metal and chalcogen are put in two quartz boats separately. A two-heating-zone splitting tubular furnace is used to control the temperature accurately at chalcogen precursor zone and metal precursor zone separately.

The fluorophlogopite mica and c-face sapphire substrates are applied to grow ReS_2 and $ReSe_2$. The 300 nm SiO_2/Si substrates are used to grow MoS_2. The newly exfoliated surface of fluorophlogopite mica, polished surface of c-face sapphire and 300 nm SiO_2/Si face to the metal precursor and located on downstream heating zone. The chalcogen precursor is set on the upstream heating zone.

Prior to the temperature ramping up, argon (300 sccm) gas is purged through the quartz tube for 10 minutes. During the deposition process, argon gas (80 sccm) is as the carrier gas to transport chalcogen vapour to the substrate location. 2 sccm H_2 gas mixed with argon gas is injected during $ReSe_2$ growth. The upstream heating zone is ramped to 200 °C and 400 °C for

sulphur powder and selenium pellets, respectively. Meanwhile, the downstream heating-zone reached 800 °C for ReS_2 and MoS_2 growth and 650 °C for $ReSe_2$ growth in 30 minutes and then held for 10 minutes. Upon completion of the temperature program, the chamber lid is opened immediately to achieve rapid cooling.

*Synthesis of graphene:*The 1L graphene is synthesized on copper foil using the atmospheric CVD system at 1097 °C. The mixed gas of H_2: Ar: CH_4 = 50: 1000: 5.5 is used. The copper foil is annealed at 1075 °C for 12 hours and subsequently processed the mechanical chemical polishing as substrate pre-treatment. The rapid cooling is applied to graphene synthesis as well.

*Transfer of CVD ReS_2 and graphene:*The wet transfer is applied to transfer CVD grown ReS_2 on fluorophlogopite mica onto a TEM grid and 300 nm SiO_2/Si in this work. Initially, liquid Poly (methyl methacrylate) (PMMA) is dropped and spin-coated on the as-grown 1L-ReS_2/mica (3000 r.p.m., 50 seconds). After PMMA curing under room temperature, it forms PMMA thin film on the surface of ReS_2 flakes (PMMA/ReS_2). Subsequently, the PMMA/ReS_2 film detaches from mica substrate by emerging in 75 °C ultrapure water for one hour. Next, a 1 cm × 1 cm SiO_2/Si substrate with 300 nm thick silicon oxide layer or Quantifoil ™ TEM grid is used to scoop out the floating PMMA/ ReS_2 layer. After PMMA/ReS_2 drying and attaching totally on the target substrates at room temperature, the acetone is introduced to remove PMMA film on SiO_2/Si and the acetone evaporation is used to get rid of the PMMA on TEM grid.

The CVD grown graphene on copper foil (graphene/Cu) is transferred onto 300 nm SiO_2/Si substrates assisted by wet transfer. The graphene/Cu is spin-coated with PMMA firstly then dipped in the Cu etching solution ($FeCl_3$/HCl, Sigma) for 30 minutes to etch away the Cu foil. Next, the PMMA/graphene is scooped up and transferred into ultrapure water to remove the etching solution for 10 minutes. Subsequently, the cleaned 300 nm SiO_2/Si substrate is used to scoop out the PMMA/graphene film. Upon the film drying and attaching on the substrate, the acetone is applied to remove PMMA.

Ultraviolet (UV) treatment method: 1L-ReS_2 flakes are placed in a chamber equipped with lamp emission light at 254 nm and 10% 185 nm mixed wavelength. Via connecting with a humidifier and N_2 gas injection, the humid level is controlled at 60% monitored by a hydro-thermometer (accuracy ± 3%). The UV treatment on 1L-ReS_2 is separated into three periods, the first period accumulates by 30 s, 60 s, 90 s UV treatment, the second period lasts 120 s and the final period keeps 150 s UV treatment. Radicals are generated under UV exposure and damp condition given by:

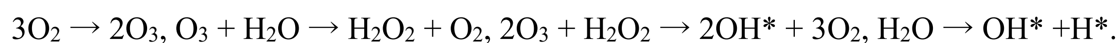

$$3O_2 \rightarrow 2O_3,\ O_3 + H_2O \rightarrow H_2O_2 + O_2,\ 2O_3 + H_2O_2 \rightarrow 2OH^* + 3O_2,\ H_2O \rightarrow OH^* + H^*.$$

In addition to 1L-ReS_2, Figure S32 shows the results of UV treated 1L-graphene samples.

Laser irradiation: The laser irradiation is performed under the same system with Raman and PL measurement. The laser spot is ~ 1 μm diameter. The laser power is adjustable ranging from 0.007 mW to 6.11 mW. The laser at different wavelength is applied to perform the laser irradiation. During laser irradiation experiment on ReS_2 and $ReSe_2$, the laser at wavelength of 633 nm is used. The laser at wavelength of 514 nm is applied to perform the laser irradiation experiment on ReS_2, MoS_2 and graphene.

Raman and photoluminescence (PL) spectra measurement: Raman spectra of ReS_2 and $ReSe_2$ are measured with a commercial inVia confocal Raman instrument (Renishaw, UK) using the excitation wavelength of 633 nm (0.57 mW), the Raman spectra of MoS_2 and graphene are recorded using the excitation wavelength of 514 nm (0.54 mW) with a grating of 1800 g mm^{-1}. The spectra are obtained under 50 × lens (0.75 N.A.) with a laser spot diameter ~ 1 μm. The laser power is calibrated by a standard photodiode power sensor S121C (Thorlabs, USA). The laser exposure time for every single spectrum is 10 s. The PL spectra of ReS_2 are recorded using the excitation wavelength of 633 nm (0.57 mW). Subsequently, the Raman spectra are fitted using Gaussian contributions.[25] The PL spectra are fitted using Lorentz curves.

The in situ Raman measurement is performed in the temperature control chamber (Linkam, UK). The temperature ramping rate is controlled at 50 °C min^{-1}. At the first UV-thermal annealing circle, the 180 s UV (1st time) treated ReS_2 sample is annealed at 150 °C, 200 °C, 250 °C, 300 °C for 60 seconds. Subsequently, the ReS_2 is taken out to perform the 180 s UV (2nd time) treatment. Next, the ReS_2 is annealed at 300 °C for 60 seconds, 120 seconds and 180 seconds. The Raman spectra are collected upon the chamber cooling down naturally to room temperature.

Dynamic force microscopy (DFM) measurement: The topography and phase images of pristine, UV-treated, laser-irradiated 1L-ReS_2 are obtained by AFM5300E system (HITACHI, Japan) in cyclic contact mode. The cyclic contact mode is to reduce the measurement influence on the wrinkle morphologies comparing with contacting mode. The n-type silicon tip NSG30 (Tipsnano, Estonia) with Au coating on the reflective side is used.

During the DFM measurement, the cantilever would vertically oscillate and the phase lag is detected which is relying on the size of adsorptive power.

Scanning transmission electron microscopy (STEM) and energy dispersive spectroscopy (EDS) measurement: The STEM images of 1L-ReS_2 are performed by transmission electron microscopy (TEM) (JEOL JEM-ARM200F) with a CEOS spherical (Cs) aberration (probe) corrector. The aberration corrected STEM under 60 kV accelerating voltage is applied in this work to improve the image resolution and prevent beam damage. Average background subtracting filtering (ABSF) is applied to reduce the noise of STEM-ADF images. The probe size is *ca.* 1.5 angstrom. The EDS is applied to measure the rhenium, sulphur, oxygen atomic ratio. Each EDS spectra is acquired for 30 seconds. The EELS acquisition is completed with the Gatan Quantum™ EELS, using the same acquisition conditions for the pristine and UV treated samples, beam probe size *ca.* 1.5 angstrom, convergence angle 29 mrad, collection angle 35mrad and exposure time 2 s are applied.

Density functional theory (DFT) simulations: Spin-polarized DFT calculations are performed by using the Vienna *ab initio* Simulation Package (VASP) program package[26] within the projector augmented wave (PAW)[27] to explore geometries and electronic properties of ReS_2. The exchange-correlation interactions are described with the generalized gradient approximation (GGA)[28] in the form of the Perdew, Burke, and Ernzernhof (PBE) functional.[29] The kinetic energy cutoff for the plane-wave basis set is chosen as 450 eV, and the distance of the vacuum layer is set to be more than 15 Å, which is sufficiently large to avoid interlayer interactions. The electronic SCF tolerance is set to 10^{-5} eV. Fully relaxed geometries and lattice constant are obtained by optimizing all atomic positions until the Hellmann–Feynman forces are less than 0.02 eV $Å^{-1}$. The k-points samplings with a gamma-centred Monkhorst-Pack scheme[30] are 12×12×1 for structural optimizations and 25×25×1 for the density of states (DOS) calculations. The formation energies of O*, and OH* are calculated as reference H_2O and H_2. The Gibbs free energy change (ΔG) of O*, and OH* is evaluated by the following equation: $\Delta G = \Delta E_{DFT} + \Delta E_{ZPE} - T\Delta S$. The reaction energy ($\Delta E_{DFT}$) can be directly determined by analyzing the DFT total energies. ΔE_{ZPE} and ΔS are the zero point energy difference and the entropy difference between the adsorbed state and the gas phase obtained from previous studies,[31] and T is the room temperature (298.15 K).

X-ray photoelectron spectroscopy (XPS): XPS (VG ESCALAB 220i-XL) is performed using an Al Kα X-ray with photons energies of 1486.6 eV working under a base vacuum lower than 10^{-9} Torr. The Re 4f, S 2p and O 1s peak data are collected to investigate the oxygen grafting/removal on ReS_2 surface during UV and laser treatment.

Device fabrication: Initially, the CVD grown 1L-ReS_2 on fluorophlogopite mica is transferred onto the 300 nm SiO_2/Si substrates using wet transfer. Next, the ReS_2 on SiO_2/Si substrate is spin-coated with methyl methacrylate (MMA) mica (4000 r.p.m., 50 seconds) and dried for 1 min at 160 °C on the hot plate. Subsequently, the PMMA is spin-coated on the MMA/ReS_2 surface (4000 r.p.m., 50 seconds) and heat at 160 °C for 5 min on the hot plate. Next, the source

and drain electrode pattern is defined using the electron beam lithography system (JEOL Model JIB-4501+NPGS) on the PMMA/MMA/ReS_2 sample. The patterned sample is dipped volume ratio of 7: 3 of isopropyl alcohol (IPA): H_2O solution for 8 s as developing and subsequently dipped in DI water for 10 s as fixing, followed by the electron beam evaporation (5 nm Cr and 50 nm Au) process. Finally, the device is obtained after lift-off in acetone.

Electrical transport Measurement: The measurement on devices is carried out in a lakeshore probe station with Keithley 4200 SCS analyser under 10^{-2} torr vacuum. During measurement, the heavily doped Si is used as the gate electrode. For the field effect transistor (FET) transfer characteristic measurement, gate voltage varied from -60 V to 60 V with a step of 0.5 V, and the source drain bias is fixed at 0.5 V, 1 V, 2V and 3 V, respectively. For the FET output characteristic measurement, source drain voltage varies from -2 V to 2 V with a step of 0.05 V, and gate voltage switched from -60 V to 60 V with a step of 10 V. All the measurement conditions are fixed the same for pristine 1L-ReS_2 device, after 90 s UV treatment and after three times of 60 s laser irradiation (633 nm, 0.57 mW).

Device analysis: Threshold voltage (V_{th}) is the inflection point voltage at which the filed-effect transistor changes from the off state to the on state. In order to reduce the influence of parasitic series resistance and mobility degradation, we employed the ratio method to calculate the V_{th} in our case. We firstly plotted the ratio of source-drain current to the square root of the transconductance ($I_{ds}/g_m^{0.5}$) as a function of gate voltage (V_g), then we extrapolated in the linear region of the $I_{ds}/g_m^{0.5}$-V_g curve, and the V_{th} is the V_g axis intercept value.[32]

The field-effect electron mobility (μ_e) is calculated using equation:[33]

$$\mu_e = \frac{L}{W C_{ox} V_{ds}} \times g_m \quad (1)$$

Where L, W, C_{ox}, V_{ds} and g_m refer to channel length, channel width, capacitance of dielectric layer, source-drain bias voltage and transconductance, respectively. Specifically, the capacitance can be expressed as:

$$C_{ox} = \frac{\varepsilon_0 \varepsilon_r}{d} \quad (2)$$

In this equation, ε_0 is the vacuum permittivity, and $\varepsilon_0 = 8.85 \times 10^{-12} \mathrm{F} \cdot \mathrm{m}^{-1}$, ε_r is the relative permittivity, and ε_r=3.9 for SiO_2, d refers to the thickness of SiO_2, and d=300 nm.

Additionally, g_m represents the transconductance, and follows this formula:

$$g_m = \frac{dI_{ds}}{dV_g} \quad (3)$$

In general, the carrier concentration of 2D atomic layers can be calculated by using the parallel-plate capacitor model, and following the equation below:[31]

$$n_{2D} = C_{ox} \Delta V_g / e \quad (4)$$

Where e is the elementary charge, and ΔV_g refers to the difference between gate voltage and threshold voltage, which can be expressed as:

$$\Delta V_g = V_g - V_{th} \quad (5)$$

In particular, this equation is applicable when V_g is larger than V_{th}.

In our cases, we calculated the carrier concentration evolution of the ReS_2 devices at V_g=0 V, considering about the threshold voltage issue, we employed the differential form of ohm theorem to roughly estimate the carrier concentration, the equation applied is:

$$n = \frac{\sigma}{e \times \mu_e} \quad (6)$$

Where σ is electrical conductivity.

Supporting Information

Supporting Information is available from the Wiley Online Library or from the author.

Acknowledgements

This work was supported by National Science Foundation of China (Project No. 51872248, 21703076, 51922113), the Hong Kong Research Grant Council under Early Career Scheme (Project No. 25301018), and the Hong Kong Research Grant Council General Research Fund (Project No. 11300820, 15302419), City University of Hong Kong (Project No. 9680241, 7005259), Natural Science Foundation of Jiangsu Province of China (Project No. BK20170466), Natural Science Foundation of the Jiangsu Higher Education Institutions of China (No.18KJA140001).

Received: ((will be filled in by the editorial staff))
Revised: ((will be filled in by the editorial staff))
Published online: ((will be filled in by the editorial staff))

References

[1] a) A. Raja, A. Chaves, J. Yu, G. Arefe, H. M. Hill, A. F. Rigosi, T.C. Berkelbach, P. Nagler, C. Schüller, T. Korn, C. Nuckoll, J. Hone, L. E. Brus, T. F. Heinz, D. R. Reichaman, A. Chernikov, *Nat. Commun*. **2017**, *8*, 15251; b) A. Allain, J. H. Kang, K. Banerjee, A. Kis, *Nat. Mater.* **2015**, *14*, 1195.

[2] a) W. Shi, S. Kahn, L. Jiang, S. Y. Wang, H. Z. Tsai, D. Wong, T. Taniguchi, K. Watanabe, F. Wang, M. F. Crommie, A. Zettl, *Nat. Electron*. **2020**, *3*, 99; b) J. S. Zhang, A. Yang, X. Wu, J. V. D. Groep, P. Tang, S. Li, B. Liu, F. Shi, J. Wan, Q. Li, Y. Sun, Z. Lu, X. Zheng, G. Zhou, C. L. Wu, S. C. Zhang, M. L. Brongersma, J. L, Y. Cui, *Nat. Commun*. **2018**, *9*, 5289.

[3] a) G. Liu, W. Jin, N. Xu, *Angew. Chem. Int. Ed*. **2016**, *55*, 13384; b) F. Perreault, A. F. de Faria, M. Elimelech, *Chem. Soc. Rev.* **2015**, *44*, 5861.

[4] a) Y. Wu, L. o vorakiat, X. Qiu, J. Liu, P. Deorani, K. Banerjee, J. Son, Y. Chen, E. E. M. Chia, H. Yang, *Adv. Mater*. **2015**, *27*, 1874; b) F. Wang, P. Stepanov, M. Gray, C. N. Lau, M. E. Itkis, R. C. Haddon, Ionic liquid gating of suspended MoS_2 field effect transistor devices. *Nano Lett.* **2015**, *15*, 5284.

[5] P. Gallagher, M. Lee, T. A. Petach, S. W. Stanwyck, J. R. Williams, K. Watanabe, M. Lee, T. A. Petach, S. W. Stanwyck, J. R. Williams, K. Watanabe, *Nat. Commun*. **2015,** *6,* 6437.

[6] a) K. Cho, M. Min, T.-Y. Kim, H. Jeong, J. Pak, J. K. Kim, J. Jang, S. J. Yun, Y. H. Lee, W.-K. Hong, T. Lee, *ACS Nano* **2015**, *9*, 8044; b) J. Pető, T. Ollár, P. Vancsó, Z. I. Popov, G. Z. Magda, G. Dobrik, C. Y. Hwang, P. B. Sorokin, L. Tapaszto, *Nat. Chem.* **2018**, *10*, 1246.

[7] S. Bae, H. Kim, Y. Lee, X. F. Xu, J.-S. Park, Y. Zheng, J. Balakrishnan, T. Lei, H. R. Kim,

Y. I. Song, Y. J. Kim, K. S. Kim, B. Özyilmaz, J. H. Ahn, B. H. Hong, S. Iijima, *Nat. Nanotechnol*. **2010**, *5*, 574.

[8] S. Cho, S. Kim, J. H. Kim, J. Zhao, J. Seok, D. H. Keum, J. Baik, D.-H. Choe, K. J. Chang, K. Suenaga, S. W. Kim, Y. H. Kim, H. Yang, *Science*, **2015**, *349*, 625.

[9] D. C. Elias, R. R. Nair, T. M. G. Mohiuddin, S. V. Morozov, P. Blake, M. P. Halsall, A. C. Ferrari, D. W. Boukhvalov, M. I. Katsnelson, A. K. Geim, K. S. Novoselov, *Science* **2009**, *323*, 610.

[10] a) S. Barja, S. Refaely-Abramson, B. Schuler, D. Y. Qiu, A. Pulkin, S. Wickenburg, H. Ryu, U. M. Ugeda, C. Kastl, C. Chen, C. Hwang, A. Schwartzberg, S. Aloni, S.-K. Mo, D. F. Ogletree, M. F. Crommie, O. V. Yazyer, S. G. Louie, J. B. Neaton, A. Weber-Bargioni, *Nat. Commun*. **2019**, *10*, 3382; b) X. Chen, N. C. Berner, C. Backes, G. S. Duesberg, A. R. McDonald, *Angew. Chem. Int. Ed*. **2016**, *55*, 5803.

[11] a) S. Yu, X. Wu, Y. Wang, X. Guo, L. Tong, *Adv. Mater.* **2017**, 29, 1606128; b) L. Yang, K. Majumdar, H. Liu, Y. Du, H. Wu, M. Hatzistergos, P. Y. Hung, R. Tieckelmann, W. Tsai, C. Hobbs, P. D. Ye, *Nano Lett*. **2015,** *14*, 6275; c) S. Lei, X. Wang, B. Li, J. Kang, Y. He, A. George, L. Ge, Y. Gong, P. Dong, Z. Jin, G. Brunetto, W. Chen, Z. T. Lin, R. Baines, D. S. Galvão, J. Lou, E. Banerjee, R. Vajtai, P. Ajayan, *Nat. Nanotechnol*. **2016**, *11*, 465.

[12] a) Z. Luo, T. Yu, K. J. Kim, Z. Ni, Y. You, S. Lim, Z. Shen, S. Wang, J. Lin, *ACS Nano* **2019**, *3*, 1781; b) M. J. McAllister, J. L. Li, D. H. Adamson, H. C. Schniepp, A. A. Abdala, J. Liu, M. Herrera-Alonso, D. L. Milius, R. Car, R. K. Prud'homme I. A. Aksay, *Chem. Mater*. **2007** *19*, 4396.

[13] H. Zhong, S. Gao, J. Shi, L. Yang, *Phys. Rev. B* **2015**, *92*, 115438.

[14] X. Li, F. Cui, Q. Feng, G. Wang, X. Xu, J. Wu, N. Mao, X. Liang, Z. Zhang, J. Zhang, H. Xu, *Nanoscale* **2016**, *8*, 18956.

[15] a) D. A. Schmidt, T. Ohta, T. E. Beechem, *Phys. Revi.* **2011**, *84*, 235422; b) S. Kataria, S. Wagner, T. Cusati, A. Fortunelli, G. Iannaccone, H. Pandey, G. Fiori, M. C. Lemme, *Adv.*

Mater. Interfaces **2017**, *4*, 1700031.

[16] a) X. Wang, M. Zhao, D. D. Nolte, *Appl. Phys. Lett.* **2009**, *95*, 081102; b) A. T. Davidson, and A. F. Vickers, *J. Phys. C: Solid State Phys.* **1972**, *5*, 879.

[17] F. Chen, S. O. Pehkonen, B. R. Madhumita, *Water Res*. **2002** *36*, 4203.

[18] a) K. S. Siow, L. Britcher, S. Kumar, H. J. Griesser, *Sains. Malays*. **2018**, *47*, 1913-1922; b) Y. P. Yan, H. Li, Y. B. Kang, B. Wang, T. Y. Eom, K. Y. Song, S. Nundy, M. W. Cho, C. W. Kang, P. Nakhanivej, J. Y. Lee, H. J. Lee, H. S. Park., *J. Mater. Chem. A* **2019**, *7*, 22070-22078; c) J. W. He, X. Xu, J. S. Corneille, D. W. Goodman, *Surf. Sci.* **1992**, *279*, 119; d) W. Wang, J. Zhang, Q. Zhang, S. Wan, X. Zhu, Q. Zhang, W. Wang, Y. Zhang, Y. Liu, L. Fu, *Adv. Mater.* **2018**, *30*, 1804559.

[19] J. K. Nørskov, J. Rossmeisl, A. Logadottir, L. Lindqvist, R. J. Kitchin, T. Bligaard, H. Jonsson, *J. Phys. Chem. B* **2004**, *108*, 17886.

[20] K. C. Santosh, R. C. Longo, R. M. Wallace, K. Cho, *J. Appl. Phys*. **2015**, *117*, 135301.

[21] T. H. Ly, Q. Deng, M. H. Doan, L.-J. Li, J. Zhao, *ACS Appl. Mater. Interfaces*. **2018**, *10*, 29893.

[22] J. Shim, A. Oh, D. H. Kang, S. Oh, S. K. Jang, J. Jeon, M. H. Jeon, M. Kim, C. Choi, J. Lee, S. Lee, G. Y. Yeom, Y. J. Song, J. H. Park, *Adv Mater.* **2016** *28*, 6985.

[23] T. H. Ly, S. J. Yun, Q. H. Thi, J. Zhao, *ACS Nano* **2017**, *11*, 7534.

[24] X. Wang, K. Shinokita, Y. Miyauchi, N. T. Cuong, S. Okada, K. Matsuda, *Adv. Funct. Mater.* **2019** *29*, 1905961.

[25] a) D. Wolverson, S. Crampin, A. S. Kazemi, A. Ilie, S. J. Bending, *ACS Nano* **2014,** *8*, 11154; b) C. Rice, R. J. Young, R. Zan, U. Bangert, D. Wolverson, T. Georgiou, R. Jalil, K. S. Novoselov, *Phys. Rev. B* **2013**, *87*, 081307.

[26] a) G. Kresse, J. Furthmüller, *Comput. Mat. Sci*. **1996**, *6*, 15; b) Kresse, G., and Furthmüller, *Phys. Rev. B* **1996**, *54*, 11169.

[27] P. E. Blöchl, *Phys. Rev. B* **1994**, *50*, 17953.

[28] J. P. Perdew, K. Burke, M. Ernzerhof, *Phys. Rev. Lett*. **1996**, *77*, 3865.

[29] J. P. Perdew, M. Ernzerhof, K. Burke, *J. Chem. Phys*. **1996**, *105*, 9982.

[30] H. J. Monkhorst, J. D. Pack, *Phys. Rev. B* **1976**, *13*, 5188.

[31] Q. Deng, J. Zhao, T. Wu, G. Chen, H. A. Hansen, T. Vegge, *J. Catal*. **2019**, *370*, 378.

[32] A. Ortiz-Conde, F. J. G. Sánchez, J. J. Liou, A. Cerdeira, M. Estrada, Y. Yue,. *Microelectron. Reliab.* **2002**, *42*, 583.

[33] P. Luo, F. Zhuge, F. Wang, L. Lian, K. Liu, J. Zhang, T Zhai, *Acs Nano* **2019**, *13*, 9028.

[34] B. Radisavljevic, A. Kis, *Nat. Mater*. **2013**, *12*, 815.

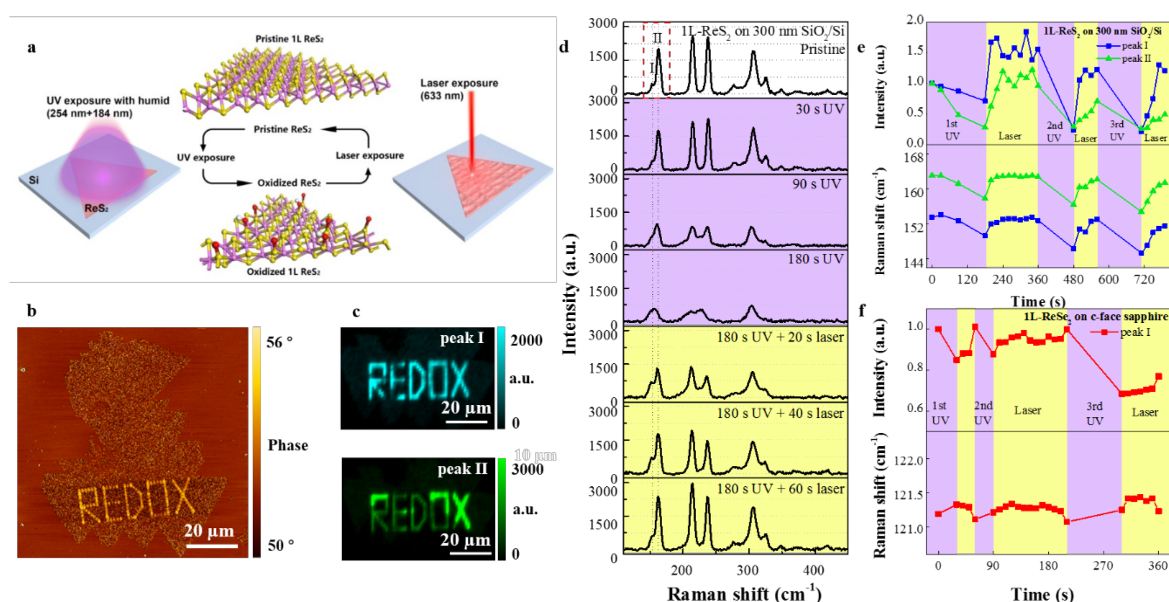

Figure 1. Reversible photochemistry on 1L-ReS_2 and 1L-$ReSe_2$. a) The schematic illustration of UV treatment under moisture condition and laser irradiation process. b) The DFM phase image of the laser irradiated "REDOX" pattern on 180 s UV treated 1L-ReS_2 grown on fluorophlogopite mica. c) The Raman intensity mapping of peak I and II corresponding to the laser irradiated pattern in (b). d) The Raman spectra of UV effect on ReS_2 and subsequent laser effect. e, f) Time evolution of Raman peaks cycled UV exposure and laser irradiations of 1L-ReS_2 on 300 nm SiO_2/Si substrate and 1L-$ReSe_2$ on c-face sapphire, respectively.

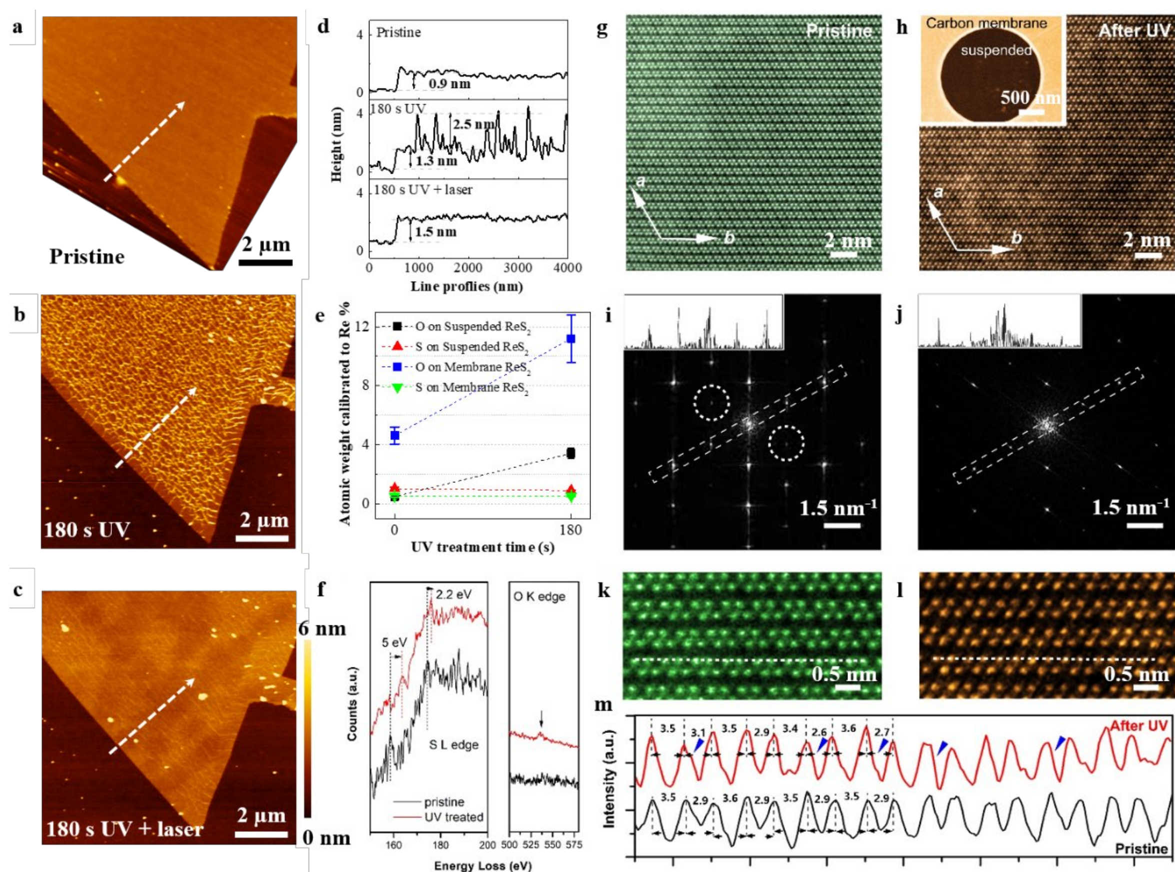

Figure 2. Analysis of photochemical effect on 1L-ReS_2. a-c) DFM topography images of pristine, 180 s UV treated, laser line scanned 1L-ReS_2 on 300nm SiO_2/Si substrate. d) The height profiles corresponding to dash lines with arrow in a-c respectively. e) EDS statistics of oxygen and sulphur atomic weight calibrated Re% pre- and post-UV treatment. f) EELS spectra of pristine and post-UV 1L-ReS_2. g, h) The high-magnification HAADF STEM images of pristine and post-UV treatment ReS_2, respectively. Inset of (h) shows the low-magnification STEM image of post-UV treatment 1L-ReS_2 on carbon film of TEM grid. i, j) Fast Fourier Transformed (FFT) reflexes for pristine and post-UV treatment 1L-ReS_2, respectively. Dashed circles in i highlighted the reflexes present in (i) but absent in (j). Insets showed the integrated intensity profiles corresponding to dashed rectangles in (i) and (j), respectively. k, l) Zoom-in HAADF images in (g) and (h), respectively. m) Intensity profiles along white dashed lines in k and l, corresponding to pristine and UV treated sample. Peak-to-peak distances (unit: angstrom) are shown for adjacent Re-Re pairing distances. Blue triangles highlighted large lattice distorted positions.

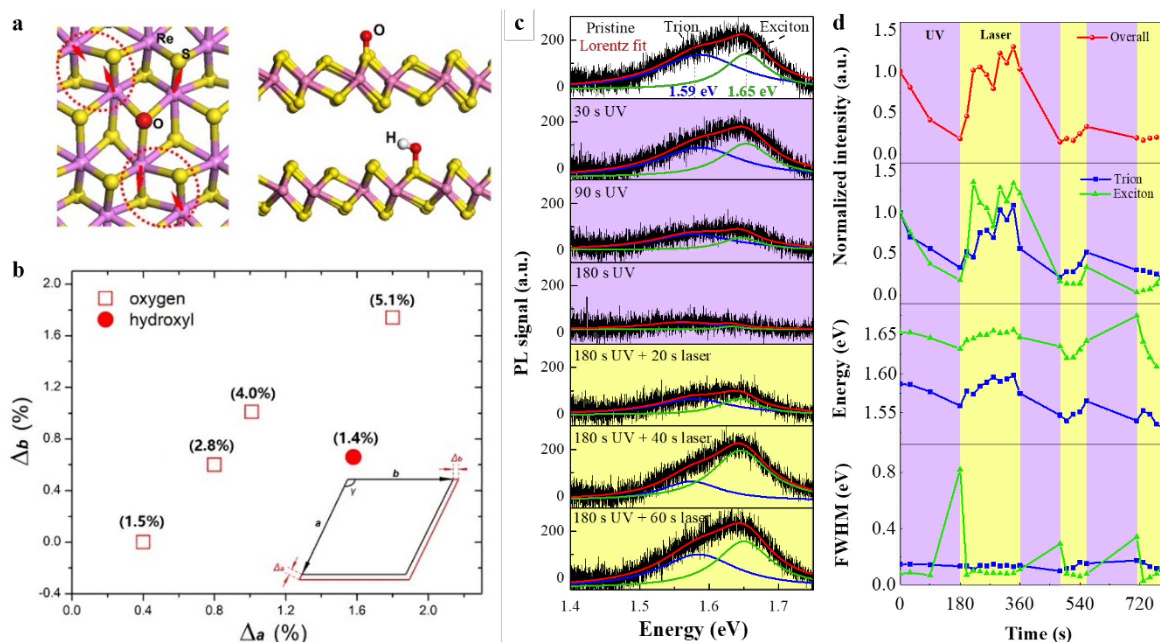

Figure 3. The DFT simulation results and PL evolutions. a) DFT Relaxed atomic structure in vicinity of a grafted O atom (top view) is shown on the left. Red arrows marked the adjacent Re atoms movement after oxidation. Red dashed circles highlighted the bonding contraction pairs. The side views of oxygen (up) and hydroxyl (down) functionalized 1L-ReS_2 are shown on the right. b) The calculated results of lattice expansion along *a* and *b* directions (basis vector of 1L-ReS_2) by oxygen and hydroxyl functionalization, weight contents of oxygen shown in brackets. The inset is the schematic of lattice expansion along *a* and *b* directions. c) Time evolution of PL spectra of 1L-ReS_2 obtained by UV treatment and laser irradiation. d) Normalized overall intensity (red curve), as well of peaks intensity, position and the full width of half maximum of trion and exciton (blue and green curves) during UV exposure and laser irradiation time.

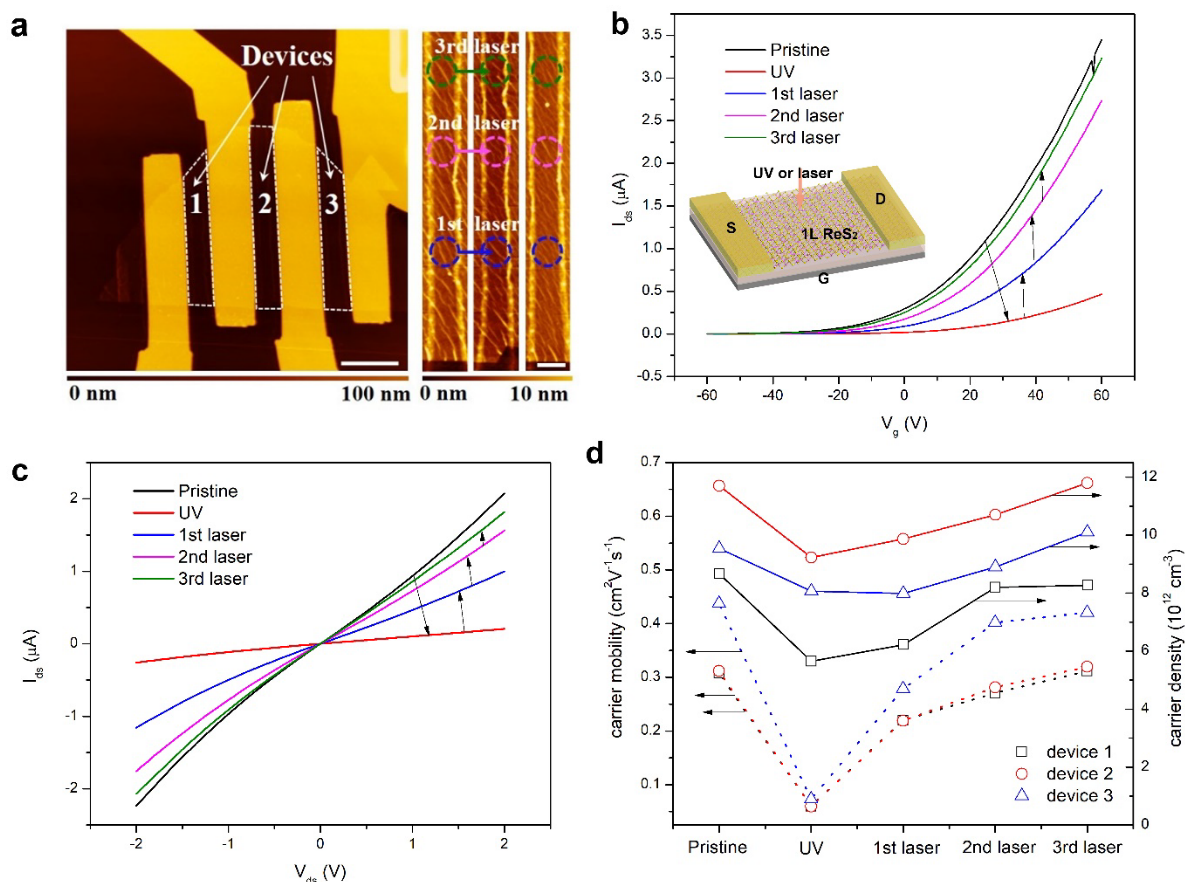

Figure 4. The tunable electrical transport properties by photochemical doping. a) The overview DFM topography image of on 90 s UV treated 1L-ReS_2 device (left). The DFM topography images of 60 s laser (633 nm, 0.57 mW) irradiated devices. (right) The locations of the first, second and third laser-irradiated spots are marked by blue, purple and green dashed circles in devices along the arrow directions, respectively. b) The transfer characteristic (I_{ds}-V_g) curves at V_{ds}=3 V for device no.1 in a, inset shows the FET device structure. c) The output characteristic (I_{ds}-V_{ds}) curves at V_g=60 V for device no.1 in (a). d) The summarized carrier mobility and carrier density dependent on the photochemical treatments. See Figures S28-S30 and Tables S1-S3 for the full set of FET device results.

Table of contents entry:

The UV/laser irradiation is employed for reversible functionalization on two-dimensional ReS_2 and $ReSe_2$ evidenced by Raman spectroscopy, dynamic force microscopy (DFM), transmission electron microscopy (TEM) and X-ray photoelectron spectroscopy (XPS). This photochemical approach without atomic defects involved are highly controllable and can effectively modulate the electrical, optical and chemical properties in these 2D semiconductors.

Keyword: (redox, photochemistry, two-dimensional materials, anisotropic, reversible doping)

Authors: Lingli Huang, Tiefeng Yang, Lok Wing Wong, Fangyuan Zheng, Xin Chen, Ka Hei Lai, Haijun Liu, Quoc Huy Thi, Dong Shen, Chun-Sing Lee, Qingming Deng*, Jiong Zhao*, Thuc Hue Ly*

Title: Redox photochemistry on van der Waals surfaces for reversible doping in two-dimensional materials

ToC figure: